Clocking Auger electrons

D. C. Haynes [1,2,3 ✉], M. Wurzer[4], A. Schletter[4], A. Al-Haddad[5,6], C. Blaga[7,8], C. Bostedt[5,6,9], J. Bozek [10], H. Bromberger[2,11], M. Bucher [6], A. Camper [7], S. Carron[12], R. Coffee[12], J. T. Costello [13], L. F. DiMauro[7], Y. Ding [12], K. Ferguson[12], I. Grguraš[1,2], W. Helml [4,14], M. C. Hoffmann [12], M. Ilchen[15,16], S. Jalas[17], N. M. Kabachnik[15,18], A. K. Kazansky[19,20,21], R. Kienberger[4], A. R. Maier [2,17], T. Maxwell [12], T. Mazza[15], M. Meyer[15], H. Park[7], J. Robinson[12], C. Roedig[7], H. Schlarb[11], R. Singla[1,2], F. Tellkamp[1,2], P. A. Walker[2,17], K. Zhang[7], G. Doumy[6], C. Behrens[11] and A. L. Cavalieri [1,2,3,5,22 ✉]

Intense X-ray free-electron lasers (XFELs) can rapidly excite matter, leaving it in inherently unstable states that decay on femtosecond timescales. The relaxation occurs primarily via Auger emission, so excited-state observations are constrained by Auger decay. In situ measurement of this process is therefore crucial, yet it has thus far remained elusive in XFELs owing to inherent timing and phase jitter, which can be orders of magnitude larger than the timescale of Auger decay. Here we develop an approach termed 'self-referenced attosecond streaking' that provides subfemtosecond resolution in spite of jitter, enabling time-domain measurement of the delay between photoemission and Auger emission in atomic neon excited by intense, femtosecond pulses from an XFEL. Using a fully quantum-mechanical description that treats the ionization, core-hole formation and Auger emission as a single process, the observed delay yields an Auger decay lifetime of $2.2^{+0.2}_{-0.3}$ fs for the KLL decay channel.

The motion of electrons underpins many of the fastest processes in atomic, molecular and condensed matter systems. In recent decades, electron transport has been the subject of intense scrutiny, thanks in large part to concurrent advances in ultrafast lasers and corresponding spectroscopic techniques. Still more recently, the exploitation of high-harmonic-generation-based extreme-ultraviolet (XUV) sources has enabled the interrogation of matter with unprecedented time resolution. However, XUV sources lack the requisite intensity to create highly excited states of matter, many of which are driven by multi-photon processes. The advent of XFELs—which occurred in parallel to advances in table-top XUV sources—has now made it feasible to excite and investigate these states, leading to pioneering techniques including double-core-hole spectroscopy[1] and the XFEL-pumped X-ray laser[2,3]. In many cases the evolution of such highly excited systems can be characterized in terms of short-lived core holes and their decay.

Auger decay is a fundamental manifestation of correlated electron dynamics, wherein the action of one electron affects another. In this process a tightly bound electron in an atom or molecule is ejected, either by absorption of an X-ray photon or collision with an energetic particle. When a more weakly bound electron fills the resulting core-hole, the energy released by this relaxation process can induce ejection of another electron, known as an Auger electron[4].

This non-radiative process is the dominant decay mechanism for elements with a low atomic number. In these cases, the core-hole decay lifetime is essentially equivalent to the Auger decay lifetime, and on the order of femtoseconds[5–7]. When the core-hole is created by photoionization, the Auger decay lifetime is related by the uncertainty principle to the spectral linewidth of the photoemission line[7–9]. High-resolution electron spectra, mostly measured using high-brightness synchrotron sources[4,8,10], have therefore been used to infer Auger decay lifetimes.

Alternatively, it is possible to access these dynamics directly in the time domain, using X-ray pulses with a duration comparable to, or shorter than, the Auger decay lifetime. For example, in proof-of-principle experiments in krypton[5] using relatively weak, table-top attosecond XUV pulses[11–13], core-holes were created by photoionization. The corresponding Auger decay was then temporally resolved by dressing the electron emission with an optical laser pulse. In these experiments, the photoemission profile essentially matches the temporal profile of the exciting attosecond XUV pulse, as photoemission occurs on attosecond timescales[14]. In contrast, the Auger emission is extended over a longer duration—typically on a femtosecond timescale.

In a number of attosecond investigations of Auger decay[15–18], the temporal profile of Auger emission has been approximated by a convolution of the XUV pulse profile with an exponential decay curve. This phenomenological ad hoc model using rate equations is based

[1]Max Planck Institute for the Structure and Dynamics of Matter, Hamburg, Germany. [2]Center for Free-Electron Laser Science, Hamburg, Germany. [3]The Hamburg Centre for Ultrafast Imaging, Universität Hamburg, Hamburg, Germany. [4]Physics Department, Technische Universität München, Garching, Germany. [5]Paul Scherrer Institute, Villigen, Switzerland. [6]Chemical Sciences and Engineering Division, Argonne National Laboratory, Lemont, IL, USA. [7]The Ohio State University, Columbus, OH, USA. [8]Kansas State University, Manhattan, KS, USA. [9]LUXS Laboratory for Ultrafast X-ray Sciences, Institute of Chemical Sciences and Engineering, Ecole Polytechnique Fédérale de Lausanne (EPFL), Lausanne, Switzerland. [10]Synchrotron SOLEIL, Gif-sur-Yvette, France. [11]Deutsches Elektronen-Synchrotron, Hamburg, Germany. [12]Linac Coherent Light Source/SLAC National Accelerator Laboratory, Menlo Park, CA, USA. [13]National Center for Plasma Science and Technology and School of Physical Sciences, Dublin City University, Dublin, Ireland. [14]Technische Universität Dortmund, Dortmund, Germany. [15]European XFEL GmbH, Schenefeld, Germany. [16]Institut für Physik and CINSaT, Universität Kassel, Kassel, Germany. [17]Department of Physics, Universität Hamburg, Hamburg, Germany. [18]Skobeltsyn Institute of Nuclear Physics, Lomonosov Moscow State University, Moscow, Russia. [19]University of the Basque Country, San Sebastián, Spain. [20]Donostia International Physics Center, San Sebastián, Spain. [21]IKERBASQUE, Basque Foundation for Science, Bilbao, Spain. [22]Institute of Applied Physics, University of Bern, Bern, Switzerland. ✉e-mail: daniel.haynes@mpsd.mpg.de; adrian.cavalieri@iap.unibe.ch

on a two-step description of Auger decay, and treats the ionization and Auger emission as distinct processes. More recently, an alternative, fully quantum-mechanical model has been proposed[19,20], which treats the time-dependent Schrödinger equation within the strong-field approximation. Within this approach, the Auger process is considered as a single-step excitation-decay of the vacancy, or Auger, state. Both creation of the vacancy and its subsequent decay into the non-stationary wavepacket of the Auger electron are considered as a single quantum-mechanical process. A similar approach was developed earlier for resonant Auger processes in molecules[21,22]. The quantum-mechanical model treats Auger decay in terms of the amplitudes of the states involved—that is, the vacancy state and the continuum of states of emitted Auger electrons—while the ad hoc rate-equation approach treats the process in terms of the real-valued populations of those states. The two models give similar results when the exciting pulse is much shorter than the Auger lifetime. However, as the exciting X-ray pulse becomes comparable to or even longer than the Auger decay lifetime, a substantial difference appears in the emission profiles predicted by the two models.

In the context of our experiment, the difference in the emission profiles is manifested in terms of the quantity we intend to measure: the time delay between the centres of mass of the photoemission and Auger emission bursts. The profiles predicted by the ad hoc two-step model have their centres of mass displaced exactly by the Auger decay lifetime, but this is not so in the quantum-mechanical model we used to determine our final results, and we must perform an additional step to retrieve the decay lifetime from the observed time delay.

In this paper, we present an experimental study of photoinduced Auger emission in the time domain, using intense, femtosecond soft X-ray pulses from an XFEL of duration commensurate with the core-hole lifetime. Under these conditions, the ad hoc two-step model fails, and a full quantum-mechanical treatment must be used, resulting in an Auger decay lifetime that is consistent with past high-resolution spectroscopic measurements. Therefore, our work represents an experimental demonstration of the quantum effect in the delay between photoionization and Auger decay, and emphasizes the general importance of treating the Auger process as a single-step quantum-mechanical process when performing future XFEL experiments.

Ultrafast science at XFELs

XFELs provide extremely intense pulses across the soft and hard X-ray spectral domains, permitting the interrogation of a wide range of systems that are not accessible via other X-ray light sources. In principle, the pulses delivered at XFELs can be short enough to explore few- or even subfemtosecond dynamics[23], including Auger decay[24]. Furthermore, XFEL pulses are many orders of magnitude more intense than X-rays from other sources, and consequently can be used to pump and probe highly excited states of matter[1–3,25–32], many of which are constrained or influenced by Auger decay.

Despite these favourable characteristics, existing attosecond time-resolved spectroscopies have hitherto been impossible to apply at XFELs. Even with modern electronic and optically distributed reference signals[33,34], it is currently not feasible to perfectly synchronize an XFEL pulse with the field of a streaking laser pulse; experiments at XFELs suffer from ever-present timing and phase jitter which places limits on the achievable time resolution. Independent time-of-arrival measurements can be used in post-processing to dramatically improve the effective time resolution[35–41], but their implementation is challenging, and in many cases the jitter remains more than an order of magnitude larger than the timescales of Auger decay. The past decade has seen the establishment of the atto-clock technique[42], based upon angular streaking, which offers an alternative to linear streaking for the attainment of few-attosecond resolution using a table-top source. Recent efforts to apply angular streaking at XFELs have shown promise as a diagnostic tool for mitigating jitter[43], but these techniques have yet to see broader application for experimental measurements at XFEL facilities.

As a result, direct time-resolved studies of most electron dynamics at XFELs have generally not yet been accomplished. There is thus a need for a straightforward technique that can unite the advantages of two very disparate light sources: whereas XFELs are the only sources able to deliver intense, ultrashort X-ray pulses and create highly excited states of matter, it is so far primarily table-top attosecond sources that have been able to provide adequate time resolution with which to probe the electronic dynamics underpinning those states.

Here, we develop and use a self-referenced streaking approach that circumvents timing jitter and allows for the extension of table-top attosecond spectroscopy to XFELs. This will enable a class of experiments benefiting from highly intense X-ray pulses alongside attosecond time resolution. As a demonstration, we have measured the delay between photoemission and Auger emission for KLL Auger decay in atomic neon, enabling us to deduce the Auger decay lifetime of K-shell vacancies in neon. These measurements were made in the time domain and with subfemtosecond precision, paving the way for the extension of the technique to a variety of ultrafast measurements at XFELs worldwide.

Time-resolved electron spectroscopy

A schematic of the experimental apparatus at the Linac Coherent Light Source free-electron laser is shown in Fig. 1. We induce $1s$ core-level photoemission and subsequent Auger decay with an XFEL pulse whose photon energy is centred at 1,130 eV with 5 eV of bandwidth. From the average pulse energy, the fluence is estimated to be below 40 J cm^{-2}. The pulse is directed into a dilute neon gas target, and the photoelectrons and Auger electrons are analysed using a time-of-flight spectrometer equipped with an electrostatic lens to increase the collection efficiency. We perform single-shot measurements of both peaks simultaneously, taking advantage of the fact that the KLL Auger spectrum of neon is dominated by the strong emission line associated with the Ne^{2+} $2p^4$ $^1D_2$ final state[44]. Acquiring both peaks simultaneously requires that they be sufficiently close together in energy; indeed, our spectral resolution is lower on the Auger peak than on the photoelectron peak owing to its higher kinetic energy.

An important prerequisite for streaking measurements is that the dynamics must occur within a half-cycle of the streaking laser field[11,45]. From the peak current in the bunch compressor, the X-ray pulse duration in our experiment was estimated to be less than 10 fs full-width at half-maximum (FWHM), so that an infrared streaking field with a correspondingly long optical cycle is required. To this end, a titanium:sapphire 800 nm femtosecond laser is used as the pump source to generate the infrared signal and idler pulses in a barium borate crystal via optical parametric amplification. These pulses are mixed in a gallium selenide crystal for difference-frequency generation, producing mid-infrared streaking pulses with a wavelength of 17 μm. The streaking period, therefore, is 57 fs, so we can be confident that the exciting X-ray pulse and the few-femtosecond Auger dynamics will be fully encompassed within a half-cycle of the streaking field.
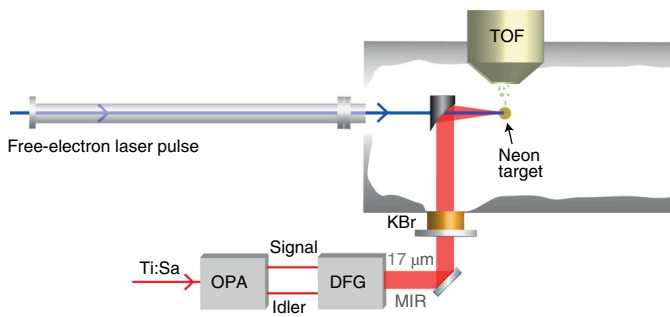
The linearly polarized streaking laser has a time-dependent electric field

$$E_{IR}(t) = E_0(t) \cos(\omega_{IR} t), \tag{1}$$

and vector potential

$$A_{IR}(t) = \frac{-E_0(t)}{\omega_{IR}} \sin(\omega_{IR} t), \tag{2}$$

such that $E_{IR}(t) = -\frac{\partial A}{\partial t}$. The symbols $E_0(t)$ and ω_{IR} represent the slowly varying amplitude of the streaking field and its angular frequency,

Fig. 1 | Mid-infrared streaking. 17 μm mid-infrared (MIR) streaking laser pulses are generated by downconversion of a near-infrared titanium:sapphire (Ti:Sa) laser pulse, using an optical parametric amplifier (OPA) and difference frequency generation (DFG), and coupled into a chamber through a potassium bromide (KBr) window. The mid-infrared pulses are focused with a parabola of focal length 100 mm and overlapped with 7 fs, 1,130 eV free-electron laser pulses in a neon gas target. The resultant streaked photo and Auger electron emission is measured using a large-acceptance time-of-flight (TOF) spectrometer.

respectively. In this experiment the maximum amplitude of the streaking field is around 5.6 MV m⁻¹, and the corresponding intensity is 40 GW cm⁻².

Upon interaction with the streaking laser field, the emitted photoelectrons' change in kinetic energy ΔE_{1s} can be approximated by

$$\Delta E_{1s} \approx \sin(\theta_i)\sqrt{8E_{el}U_p}, \tag{3}$$

where θ_i is the phase of the streaking pulse at the moment of photoemission t_i and E_{el} is the electrons' field-free kinetic energy[46,47]. This equation is central to streaking spectroscopy and follows from the classical expression for the electron kinetic energy in the laser field[46] with the condition that $U_p \ll E_{el}$. The ponderomotive potential U_p is given by

$$U_p = \frac{e^2 E_0^2}{4m_e \omega_{IR}^2}, \tag{4}$$

where e and m_e are the charge and mass of the electron. Examination of equations (2)–(4) reveals that the change in the final kinetic energy ΔE experienced by the observed electron is proportional to the vector potential $A(t)$ of the streaking field at the moment of interaction. For extended emission, the streaking laser in effect maps the time domain onto the sheared electron spectrum. This approach provides a route towards reconstructing the temporal characteristics of the electron emission with the potential for attosecond resolution[11,46]. A crucial requirement is that the amplitude and phase of the streaking field acting on the emitted electrons must be known with sufficient precision.

Self-referenced streaking spectroscopy

Using our experimental technique, we can potentially determine both the amplitude and phase of the streaking laser field for each shot by simultaneously measuring shifts in the kinetic energy of two types of electrons. In this experiment, we observe the kinetic energies of both the photoemission and Auger peaks after interaction with the streaking laser. We note that, whereas the photoelectrons and Auger electrons are both shifted in kinetic energy according to equation (3), the Auger electrons are generally emitted later than the photoelectrons. As a result, the phase of the streaking laser will have advanced by some amount in the time between emissions, owing to the pulse's propagation through the stationary target. Consequently, the Auger electrons' energy shift will be a function not only of θ_i,

but of $\theta_i + \theta_A$, where θ_A represents the phase advance between the instants of photoemission and Auger emission. The result is that the change in energy experienced by photoelectrons and Auger electrons will generally differ in magnitude and even sign, depending on the temporal overlap and absolute carrier-envelope phase of the mid-infrared pulse (It should be noted that since the field-free kinetic energies E_{el} of the two types of electrons are different, there would always be a difference in the magnitude of their energy changes, even if the emissions were simultaneous, due to the factor of $\sqrt{E_{el}}$ in equation (3)).

Conceptually, if one were to smoothly vary the overlap between X-ray-stable and carrier-envelope-phase-stable streaking pulses, the sinusoidal curves traced out by the two emission peaks' centres of energy would be temporally displaced by the time elapsed between the two events, as illustrated in Fig. 2a and Fig. 2b. In effect, each peak in the electron energy spectrum independently samples the oscillation of the streaking vector potential. When plotting the two streaked centres of energy against each other, as in Fig. 2c, the resultant ring has an ellipticity determined by the phase shift between the two sine curves. A phase shift of 0 (that is the case where both emissions were simultaneous) would result in a straight line, as both emissions would experience the same vector potential in each shot. If the shift were π/2, the graph would be a wide ellipse with major and minor axes parallel to those of the coordinate system, because whenever one emission interacted with a zero crossing of the streaking field, the other would interact with an extremum. Finally, a phase shift between 0 and π/2 would lead to a sheared ellipse.

In reality, the carrier-envelope phase of the mid-infrared streaking pulse cannot be controlled during experiments at XFELs. Therefore, each single-shot measurement is made with a random streaking phase. Nevertheless, if a large enough set of measurements is accumulated, the entire parameter space will be explored, and a scatter plot forming an ellipse like that in Fig. 2c can be constructed.

In addition to its randomly varying phase, the precise arrival time of the streaking pulse with respect to the X-ray pulse fluctuates. Therefore, the strength of the streaking effect varies from shot to shot, depending on the temporal overlap between the X-ray pulse and mid-infrared intensity pulse envelope. Whereas variation in the streaking field phase leads to the characteristic ellipse, these timing-jitter-induced variations in streaking strength result in a broadening of the elliptical distribution, since for any given angle around the ellipse there are a range of possible displacements from its centre. If the jitter were very small, the ellipse would collapse to a single line like that shown in the idealized plot in Fig. 2c. In this case, all shots would overlap with the same part of the streaking field envelope, although the carrier-envelope phase would still vary between shots. If the timing jitter increases relative to the streaking pulse duration, the centre of the ellipse becomes filled.

In principle, the shape of the ellipse may also be influenced by photon energy jitter, which causes corresponding variations in the initial kinetic energy of each burst of photoelectrons. This occurs prior to and independent of the interaction of the photoelectrons with the streaking field, and manifests as a small offset in the measured photoelectron kinetic energy spectra. The Auger spectra are immune to energy jitter, because the initial kinetic energy of the Auger electrons is independent of the X-ray photon energy.

The elliptical distribution, generated by correlating the streaking-induced shift in kinetic energy of the photoelectron and Auger peaks in single-shot measurements made over a complete set of streaking field parameters, is the key to our technique. In effect, the correlation plot is a map, with each position pinned to a unique set of streaking field parameters. Once this distribution has been obtained, all subsequent single-shot measurements can be mapped to retrieve the instantaneous streaking phase and amplitude. Single-shot measurements performed with desired streaking parameters can be identified and isolated, even though those
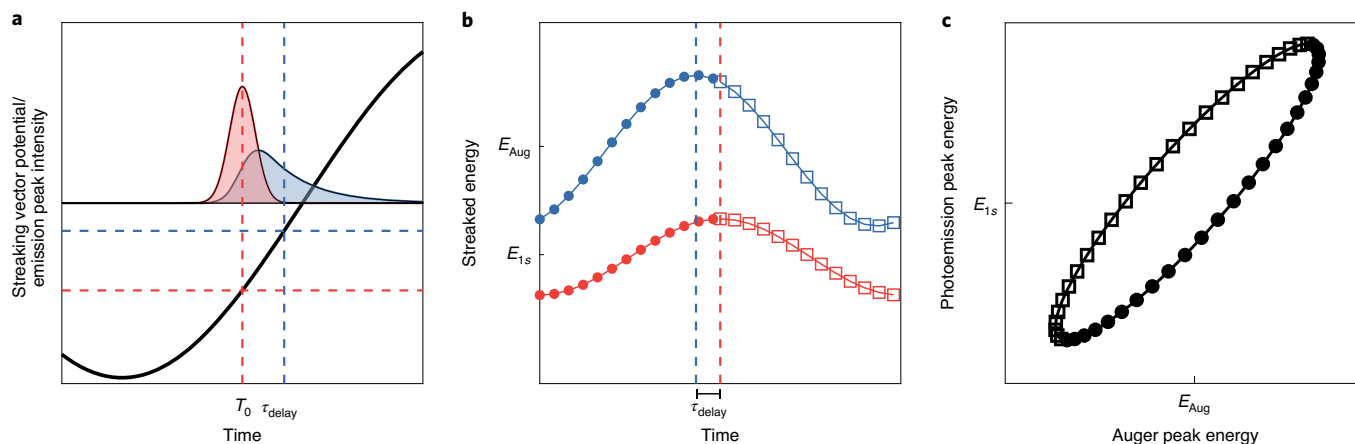
Fig. 2 | Principle of self-referenced photoionized streaking measurements. a, The photoelectrons (red) are emitted promptly after the arrival of the X-ray pulse at T_0. After the core-hole decays, the Auger electrons (blue) are emitted. The delay between the emission peaks' weighted centres, τ_{delay}, which is highlighted by the distance between the vertical dotted lines, causes each set of electrons to interact with a different phase of the streaking pulse (solid black line). The horizontal dotted lines further highlight the difference in streaking field in each case. **b**, If the temporal overlap were smoothly varied over one streaking cycle, the resultant kinetic energy of each peak would trace out sinusoidal curves, shifted by the Auger decay lifetime. Filled circles represent positive streaking slopes at the moment of ionization and open squares represent negative slopes. The dotted lines highlight the temporal overlap which results in the largest increase in kinetic energy for each peak, so that the gap between the dotted lines corresponds to the temporal shift between the two sinusoidal curves. For reference, the field-free energies of the photo- and Auger electrons are indicated by E_{Aug} and E_{1s}, respectively. **c**, Plotting each pair of positions against each other results in an ellipse. Filled circles and open squares have the same meaning as in **b**.

parameters are uncontrolled during the experiment. This is how we have extended the techniques of table-top attosecond spectroscopy to be applied at XFELs, allowing a dramatic increase in achievable time resolution to the subfemtosecond regime.

Experimental results

In the experiment, the streaked kinetic energies of the photoelectron and Auger electron peaks are determined by numerically fitting the recorded spectra in each single-shot measurement and calculating the centre of energy of each peak. In addition to the streaked measurements, we also obtained thousands of spectra in the absence of the streaking laser. By comparing the streaked energies to the corresponding streaking-field-free values, we determine the changes in kinetic energy, ΔE_{Auger} and ΔE_{1s}, induced by the streaking field in each single-shot measurement. These field-free kinetic energies can also be used to determine the photon energy jitter. In our experiments this jitter follows a distribution with a root-mean-square width of 1.2 eV, which was small in comparison to the total change in the photoelectron kinetic energy induced by the streaking field. This, in conjunction with its normally distributed nature and the fact that we average over many thousands of shots in the following treatment, allows it to be neglected. In future experiments, if the photon energy jitter were found to be non-negligible, there are multiple approaches that might be taken to mitigate or eliminate its effect. The most straightforward of these would be simultaneous reference measurements of the single-shot X-ray photon energy.

Figure 3 shows the correlation between ΔE_{Auger} and ΔE_{1s} obtained from tens of thousands of streaked measurements, revealing a characteristic elliptical distribution. Specific regions of the ellipse are highlighted, with sketches of the corresponding measurement conditions shown in the subplots on the right. The subplots indicate how the correlation map can be used to navigate to previously inaccessible streaking parameters: the angular coordinate of each point identifies the streaking phase for that shot, and its radial coordinate is a function of the streaking field amplitude.

The characteristic elliptical distribution in Fig. 3 will be used to measure the delay between photoemission and Auger emission,

which itself will be used to calculate the Auger decay lifetime. The distribution also provides access to important diagnostics.

The data in Fig. 3 make it simple to identify those shots for which the photoemission burst coincides with a zero crossing of the streaking vector potential. Such shots appear on the 'equator' of the ellipse, since the photoelectrons experienced a minimal energy shift. After identifying these shots, it is possible to calculate the average duration of the X-ray pulse by comparing the width of the photoemission line in these maximally broadened shots to the width of the field-free photoemission lines. Using this method, we determined the average X-ray pulse FWHM to be 7 ± 1 fs, as detailed in the Methods.

Further, by analysing the widths of the distributions in our data and given the pulse duration of the mid-infrared laser, which was approximately 300 fs root-mean-square, we calculated that the timing jitter has a root-mean-square width of 110 fs. One of the chief strengths of self-referenced streaking is that it enables resolution that would ordinarily be impossible with jitter this severe; we will use these data to measure a temporal delay with subfemtosecond precision despite the presence of timing jitter that is orders of magnitude larger.

The delay in Auger emission

As an alternative to examining features in the individual or averaged streaked Auger spectra, which is not possible here owing to limited energy resolution, the degree of ellipticity in the distribution can provide access to the delay between the two emission bursts. We note that any ellipse can be described using the set of parametric equations

$$x(\theta) = A \sin(\theta + \phi_A), \; y(\theta) = B \sin(\theta). \quad (5)$$

In our case, x and y correspond to the change in kinetic energy of the Auger and photoelectrons respectively. As described in detail in the Methods, the angle ϕ_A is the phase advance that occurs between the two instants of electron emission. It is given by

$$\phi_A = \sin^{-1}\left(\frac{y_1}{y_2}\right), \quad (6)$$
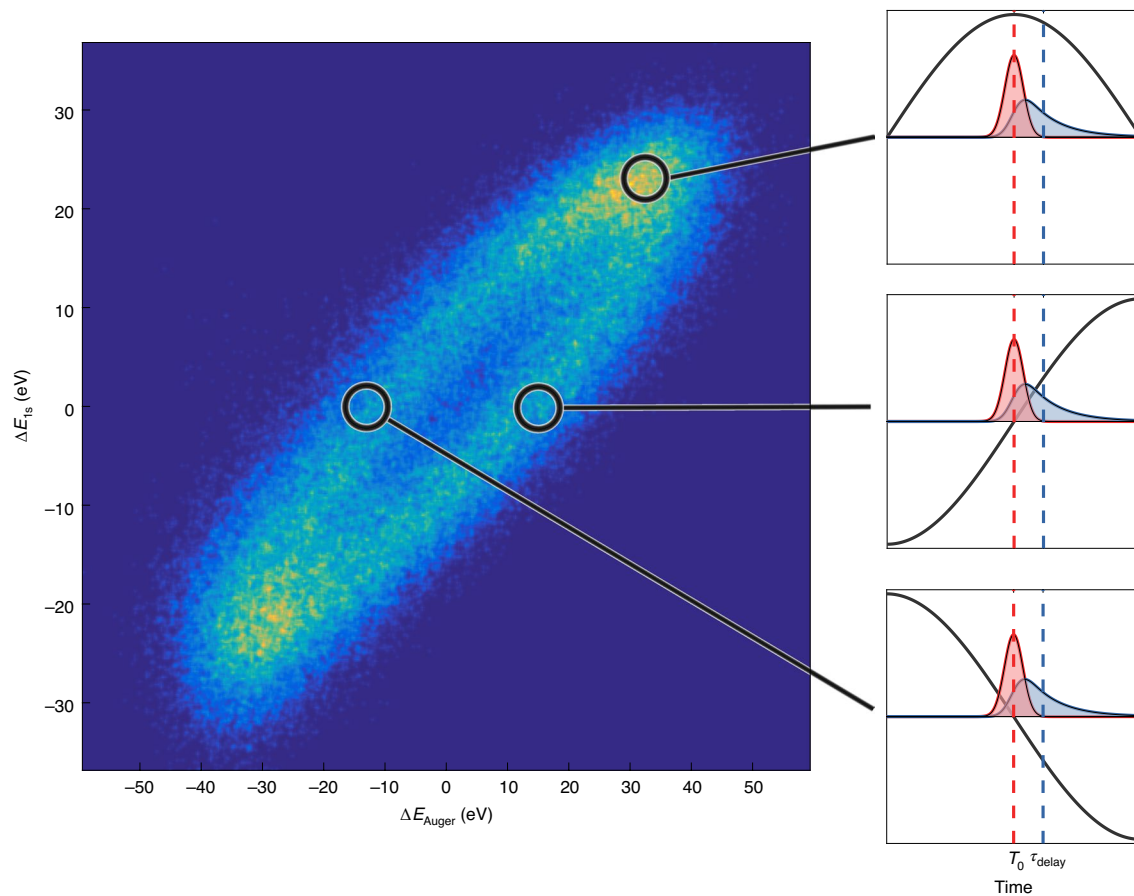
Fig. 3 | Self-referenced streaking in neon. Correlation map generated from 80,000 single-shot streaking measurements in neon using a 17 µm streaking field, and 7 fs FWHM, 1,130 eV ionizing X-ray pulses. The x and y coordinates of the individual points in the scatter plot are determined by numerically fitting the streaked kinetic energy shift of the photo- and Auger electron peaks in each shot and calculating their centres of energy. By comparing these values to the field-free kinetic energies of the peaks, we can plot the streaking-laser-induced changes in kinetic energy, ΔE_{Auger} and ΔE_{1s}, against each other. On the right, three sketches are shown, corresponding to three characteristic regions on the map. The sketches show the photoelectrons (red) and Auger electrons (blue) along with the streaking field (black). The weighted centres of each temporal emission profile are highlighted with vertical dotted lines.

where y_1 is the ellipse's y intercept, and y_2 is its maximum value of y. By examining the angular sectors of the ellipse corresponding to y_1 and y_2 we can calculate them, obtaining values of $8.0 \pm 0.1\,\text{eV}$ and $20.9 \pm 0.1\,\text{eV}$, respectively. Using these values in conjunction with equation (6) enables us to calculate the phase advance ϕ_A to be 0.39 ± 0.01 radians. Details of the selection of the sectors containing the points, and the calculation of the uncertainty on these values, can be found in the Methods. The corresponding time-delay, τ_{delay}, between the photoemission and Auger emission bursts can then be calculated using the observed phase shift ϕ_A and $T_{\text{IR}} = 56^{+3}_{-7}\,\text{fs}$, the period of the streaking pulse:

$$\tau_{\text{delay}} = \frac{\phi_A}{2\pi} T_{\text{IR}}. \qquad (7)$$

Applying this algorithm to the distribution shown in Fig. 3, we obtain a delay of $3.5^{+0.3}_{-0.5}\,\text{fs}$ The subfemtosecond uncertainty on this value was obtained by propagating the uncertainties on ϕ_A and T_{IR} using a standard functional approach, as detailed further in the Methods. Notably, by extracting information from a large amount of individual shots, our technique enables us to measure this delay despite using an X-ray pulse whose duration is longer. However, in this case, we must avoid using a theoretical model of Auger decay which assumes a very short ionizing pulse.

Evaluation of the Auger decay lifetime

We will apply a fully quantum-mechanical theoretical model of the Auger emission process to interpret our measurement of the delay between photo- and Auger emission bursts. This model of laser-assisted Auger decay was originally developed in reference[20], and is based on the solution of the time-dependent Schrödinger equation describing atomic ionization by an X-ray pulse and corresponding Auger decay in the presence of a strong laser field. A complete mathematical description can be found in the Supplementary Information.

We can use this model to calculate time-dependent Auger emission profiles and examine their dependence on experimental and physical parameters. We are interested in the time delay between the centres of mass of the photoemission and Auger emission profiles, which is the experimentally measured quantity τ_{delay}. In our calculations we find that τ_{delay} is dependent not only on the Auger decay lifetime τ_A, but also on the ionizing X-ray or XUV pulse used in the experiment. This stands in contrast to the predictions of the ad hoc two-step model used in past work[5], in which the quantities τ_{delay} and τ_A are identical regardless of ionizing pulse duration. The quantum-mechanical model shows that this is only accurate when extremely short ionizing pulses are used. In most XFEL experiments with femtosecond pulses, this condition is not met, and τ_{delay} can
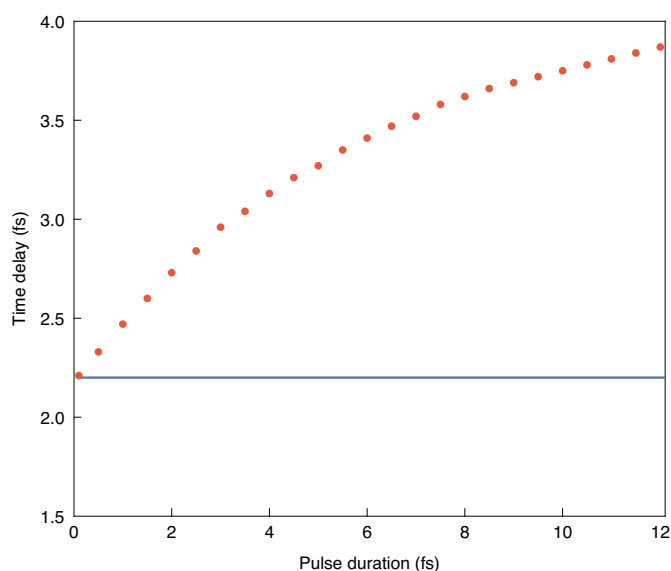
Fig. 4 | Results of simulations showing the dependence of τ_{delay} (red points) on the exciting X-ray pulse duration (FWHM). Each point was obtained by simulating the experiment using a comprehensive quantum-mechanical treatment. The blue solid line shows the Auger decay lifetime $\tau_A = 2.2$ fs, which was used for every simulation.

only be correctly related to the Auger decay lifetime by using the quantum-mechanical model.

By calculating the delays τ_{delay} associated with a variety of possible Auger decay lifetimes τ_A and accounting for the 7 ± 1 fs X-ray pulse duration measured in our experiment, the model allows us to map between τ_{delay} and τ_A. This procedure led to the conclusion that the observed delay $\tau_{delay} = 3.5^{+0.3}_{-0.5}$ fs between the emission bursts corresponds to an Auger decay lifetime $\tau_A = 2.2^{+0.2}_{-0.3}$ fs. The uncertainty on this value incorporates that on τ_{delay} and the X-ray pulse duration, which were propagated using a functional approach. Our final result for the Auger decay lifetime is in agreement with measurements reported from spectral linewidth studies, which have found values in the range 2.0–2.6 fs (refs. [7,10,48,49]).

To illustrate the importance of the theoretical model, we have performed additional simulations with variable X-ray pulse duration. Keeping the Auger decay lifetime fixed at the retrieved value of 2.2 fs, we increased the X-ray pulse duration from 100 as to 12 fs. The results are shown in Fig. 4. Although the observed delay is close to the Auger decay lifetime for attosecond pulses, a substantial difference appears as the ionizing pulse duration increases. This difference between τ_{delay} and τ_A demonstrates the necessity for a full quantum-mechanical treatment for experiments such as ours, where the exciting X-ray pulse duration is comparable to or longer than the Auger decay lifetime.

Conclusion and outlook

This measurement, which was performed at an XFEL, was made possible via self-referenced attosecond streaking. Following this successful demonstration of its efficacy, self-referenced streaking will enable experiments to take advantage of the extreme-intensity X-ray pulses at XFELs while simultaneously exploiting the unrivalled time resolution provided by attosecond streaking spectroscopy.

In conjunction with the technique, the measurement was made possible via the application of a consistent quantum model of Auger decay[20]. Through the application of this more advanced model, we demonstrated that the older, ad hoc two-step model overestimates the extracted lifetime by more than 1 fs under the present experimental conditions. This will have major ramifications for future

studies of Auger decay, especially those applying our self-referenced streaking to make the measurement at XFELs.

Because so many highly excited states of matter relax via Auger decay, this result may also help to inform future studies on double-core-hole spectroscopy[26–31], XFEL-pumped X-ray lasers[2,3], and other innovative techniques dependent upon the timescales of Auger processes. Beyond simple atomic systems, our self-referenced Auger measurements could pave the way for investigations into the effect of a system's chemical environment on Auger decay[50]; a comparison could, for example, be made between decay rates of carbon[6] in CF_4 and CO. Studies of Auger decay in molecules would require high energy resolution in order to resolve structures in these more complicated Auger spectra, and the quantum model used for the interpretation of the data would need to be expanded to encompass molecular structures. Nevertheless, this is a promising avenue for future experiments. Furthermore, we expect that precise temporal characterisation of Auger decay processes in complex systems will be crucial in interpreting diffraction and scattering patterns in single-molecule imaging experiments, where a large proportion of Auger electrons are known to deposit energy into molecular samples after emission[51,52].

Online content

Any methods, additional references, Nature Research reporting summaries, source data, extended data, supplementary information, acknowledgements, peer review information; details of author contributions and competing interests; and statements of data and code availability are available at https://doi.org/10.1038/s41567-020-01111-0.

References

1. Young, L. et al. Femtosecond electronic response of atoms to ultra-intense X-rays. *Nature* **466**, 56–61 (2010).
2. Rohringer, N. An atomic inner-shell laser pumped with an X-ray free-electron laser. *J. Phys. Conf. Ser.* **194**, 012012 (2009).
3. Rohringer, N. et al. Atomic inner-shell X-ray laser at 1.46 nanometres pumped by an X-ray free-electron laser. *Nature* **481**, 488–491 (2012).
4. Mehlhorn, W. 70 years of Auger spectroscopy, a historical perspective. *J. Electron Spectrosc. Relat. Phenom.* **93**, 1–3 (1998).
5. Drescher, M. et al. Time-resolved atomic inner-shell spectroscopy. *Nature* **419**, 803–807 (2002).
6. Carroll, T. et al. Carbon 1s photoelectron spectroscopy of CF_4 and CO: search for chemical effects on the carbon 1s hole-state lifetime. *J. Chem. Phys.* **116**, 10221 (2002).
7. Coreno, M. et al. Measurement and ab initio calculation of the Ne photoabsorption spectrum in the region of the K edge. *Phys. Rev. A* **59**, 2494–2497 (1999).
8. Jurvansuu, M. et al. Inherent lifetime widths of Ar $2p^{-1}$, Kr $3d^{-1}$, Xe $3d^{-1}$, and Xe $4d^{-1}$ states. *Phys. Rev. A* **64**, 012502 (2001).
9. Krause, M. O. Atomic radiative and radiationless yields for K and L shells. *J. Phys. Chem. Ref. Data* **8**, 307–327 (1979).
10. Schmidt, V. *Electron Spectrometry of Atoms Using Synchrotron Radiation* (Cambridge Univ. Press, 1997).
11. Kienberger, R. et al. Atomic transient recorder. *Nature* **427**, 817–821 (2004).
12. Goulielmakis, E. et al. Single-cycle nonlinear optics. *Science* **320**, 1614–1617 (2008).
13. Hentschel, M. et al. Attosecond metrology. *Nature* **414**, 509–513 (2001).
14. Schultze, M. et al. Delay in photoemission. *Science* **328**, 1658–1662 (2010).
15. Uiberacker, M. et al. Attosecond real-time observation of electron tunnelling in atoms. *Nature* **446**, 627–632 (2007).
16. Uphues, T. et al. Ion-charge-state chronoscopy of cascaded atomic Auger decay. *New J. Phys.* **10**, 25009 (2008).
17. Krikunova, M. et al. Time-resolved ion spectrometry on xenon with the jitter-compensated soft X-ray pulses of a free-electron laser. *New J. Phys.* **11**, 123019 (2009).
18. Verhoef, A. J. et al. Time- and energy-resolved measurement of Auger cascades following Kr 3d excitation by attosecond pulses. *New J. Phys.* **13**, 113003 (2011).
19. Smirnova, O., Yakovlev, V. S. & Scrinzi, A. Quantum coherence in the time-resolved Auger measurement. *Phys. Rev. Lett.* **91**, 253001 (2003).

20. Kazansky, A. K., Sazhina, I. P. & Kabachnik, N. M. Time-dependent theory of Auger decay induced by ultra-short pulses in a strong laser field. *J. Phys. B* **42**, 245601 (2009).

21. Pahl, E., Meyer, H. & Cederbaum, L. Competition between excitation and electronic decay of short-lived molecular states. *Z. Phys. D* **38**, 215–232 (1996).

22. Pahl, E., Cederbaum, L. S., Meyer, H.-D. & Tarantelli, F. Controlled interplay between decay and fragmentation in resonant Auger processes. *Phys. Rev. Lett.* **80**, 1865–1868 (1998).

23. Duris, J. et al. Tunable isolated attosecond X-ray pulses with gigawatt peak power from a free-electron laser. *Nat. Photon.* **14**, 30–36 (2020).

24. Bostedt, C. et al. Linac coherent light source: the first five years. *Rev. Mod. Phys.* **88**, 015007 (2016).

25. Yoneda, H. et al. Atomic inner-shell laser at 1.5-ångström wavelength pumped by an X-ray free-electron laser. *Nature* **524**, 446–449 (2015).

26. Fang, L. et al. Double core-hole production in N_2: beating the Auger clock. *Phys. Rev. Lett.* **105**, 083005 (2010).

27. Cederbaum, L. S. et al. On double vacancies in the core. *J. Chem. Phys.* **85**, 6513–6523 (1986).

28. Santra, R., Kryzhevoi, N. V. & Cederbaum, L. S. X-ray two-photon photoelectron spectroscopy: a theoretical study of inner-shell spectra of the organic para-aminophenol molecule. *Phys. Rev. Lett.* **103**, 013002 (2009).

29. Cederbaum, L. S. et al. Double vacancies in the core of benzene. *J. Chem. Phys.* **86**, 2168–2175 (1987).

30. Tashiro, M. et al. Molecular double core electron spectroscopy for chemical analysis. *J. Chem. Phys.* **132**, 184302 (2010).

31. Salén, P. et al. Experimental verification of the chemical sensitivity of two-site double core-hole states formed by an X-ray free-electron laser. *Phys. Rev. Lett.* **108**, 153003 (1991).

32. Ott, C. et al. Strong-field extreme-ultraviolet dressing of atomic double excitation. *Phys. Rev. Lett.* **123**, 163201 (2019).

33. Schulz, S. et al. Femtosecond all-optical synchronization of an X-ray free-electron laser. *Nat. Commun.* **6**, 5938 (2015).

34. Sato, T. et al. Femtosecond timing synchronization at megahertz repetition rates for an X-ray free-electron laser. *Optica* **7**, 716–717 (2020).

35. Schorb, S. et al. X-ray optical cross-correlator for gas-phase experiments at the Linac Coherent Light Source free-electron laser. *Appl. Phys. Lett.* **100**, 121107 (2012).

36. Grguraš, I. et al. Ultrafast X-ray pulse characterization at free-electron lasers. *Nat. Photon.* **6**, 852–857 (2012).

37. Cavalieri, A. L. et al. Clocking femtosecond X-rays. *Phys. Rev. Lett.* **94**, 114801 (2005).

38. Bionta, M. R. et al. Spectral encoding of X-ray/optical relative delay. *Opt. Express* **19**, 21855–21865 (2011).

39. Harmand, M. et al. Achieving few-femtosecond time-sorting at hard X-ray free-electron lasers. *Nat. Photon.* **7**, 215–218 (2013).

40. Hartmann, N. et al. Sub-femtosecond precision measurement of relative X-ray arrival time for free-electron lasers. *Nat. Photon.* **8**, 706–709 (2014).

41. Fung et al. Dynamics from noisy data with extreme timing uncertainty. *Nature* **532**, 471–475 (2016).

42. Eckle, P. et al. Attosecond angular streaking. *Nat. Phys.* **4**, 565–570 (2008).

43. Hartmann, N. et al. Attosecond time–energy structure of X-ray free-electron laser pulses. *Nat. Photon.* **12**, 215–220 (2018).

44. Krause, M. O., Stevie, F. A., Lewis, L. J., Carlson, T. A. & Moddeman, W. E. Multiple excitation of neon by photon and electron impact. *Phys. Lett. A* **31**, 81–82 (1970).

45. Frühling, U. et al. Single-shot terahertz-field-driven streak camera. *Nat. Photon.* **3**, 523–528 (2009).

46. Itatini, J. et al. Attosecond streak camera. *Phys. Rev. Lett.* **88**, 173903 (2002).

47. Mazza, T. et al. Sensitivity of nonlinear photoionization to resonance substructure in collective excitation. *Nat. Commun.* **6**, 6799 (2015).

48. Svensson, S. et al. Lifetime broadening and CI-resonances observed in ESCA. *Phys. Scr.* **14**, 141–147 (1976).

49. Southworth, S. H. et al. Double K-shell photoionization of neon. *Phys. Rev. A* **67**, 062712 (2003).

50. Cutler, J. N., Bancroft, G. M., Sutherland, D. G. & Tan, K. H. Chemical dependence of core-level linewidths and ligand-field splittings: high-resolution core-level photoelectron spectra of I $4d$ levels. *Phys. Rev. Lett.* **67**, 1531–1534 (1991).

51. Neutze, R. et al. Potential for biomolecular imaging with femtosecond X-ray pulses. *Nature* **406**, 752–757 (2000).

52. Gorobtsov, O. Yu., Lorenz, U., Kabachnik, N. M. & Vartanyants, I. A. Theoretical study of electronic damage in single-particle imaging experiments at X-ray free-electron lasers for pulse durations from 0.1 to 10 fs. *Phys. Rev. E* **91**, 062712 (2015).

Methods

Calculation of the average pulse duration. The duration of the X-ray pulse is an important parameter in this experiment, as it influences the emission profile of both types of electrons. We will calculate it following the methods described in ref. [53]. Our method is facilitated by the correlation plot shown in Fig. 3, and provides similar resolution to established non-invasive measurements of pulse duration[54]. In streaking experiments such as ours, the duration of an X-ray pulse can be calculated using the relation

$$\tau_{\mathrm{X}} = \frac{\sigma_{\mathrm{DC}}}{s}, \tag{8}$$

where σ_{DC} represents the breadth of the streaked photoemission peak after deconvolving that of the field-free peak, and $s = \frac{\mathrm{d}E_k}{\mathrm{d}t}$ is the streaking speed. The latter represents the rate of change of the peak's kinetic energy with respect to the timing of the streaking pulse. Where the X-ray and streaking pulses are well overlapped, the final energy of photoelectrons emitted at time t is given by

$$E_{\mathrm{k}}(t) = \frac{\Delta E_{\mathrm{max-min}}}{2} \sin(\omega_{\mathrm{IR}} t) + E_{1s}, \tag{9}$$

where $\Delta E_{\mathrm{max\text{-}min}}$ is the difference between the most positive and most negative changes in photoelectron energy throughout the experiment, ω_{IR} is the angular frequency of the streaking field, and E_{1s} is the field-free kinetic energy of the photoelectrons. Therefore, at the zero-crossing of the streaking field,

$$s = \frac{\Delta E_{\mathrm{max-min}} \times \pi}{T_{\mathrm{IR}}}, \tag{10}$$

where we have used the relation $T_{\mathrm{IR}} = \frac{2\pi}{\omega_{\mathrm{IR}}}$ and set $t = 0$.

The value of $\Delta E_{\mathrm{max\text{-}min}}$ is calculated from angular sectors corresponding to the maxima and minima of the streaking phase. All shots within a given angular sector interact with the same streaking phase, but the final kinetic energy of the electrons will still vary according to the streaking field amplitude—which will itself vary according to timing jitter. Clearly, the largest possible change in kinetic energy will occur when the streaking amplitude is maximal and the phase causes the electrons to interact with a peak of the streaking vector potential. Because timing jitter results in a normal distribution of streaking amplitudes, it is most likely that a given shot will intersect with the centre of the streaking pulse envelope. These conditions are identified by numerically fitting the distribution of absolute photoelectron kinetic energies within both sectors and extracting its peak, as shown in Extended Data Fig. 1. Using this method, we determine that $\Delta E_{\mathrm{max\text{-}min}} = 48 \pm 1$ eV.

The first step towards finding σ_{DC} is to calculate the spectral width of the photoemission peak at the zero crossing of the streaking field. These shots can be swiftly identified using the elliptical distribution: they must lie on its equator, where the kinetic energy of the photoelectrons was largely unchanged. Further, the shots closest to the edge of the ellipse interacted with the peak of the streaking pulse envelope, resulting in a maximized change in Auger electron kinetic energy. Therefore, we restrict our consideration to shots for which the final photoelectron kinetic energy was within 1 eV of its field-free value. Within this group, we take the 300 outermost shots on each side of the ellipse, corresponding to the strongest streaking effect. Recall that, as illustrated in Fig. 3, the left and right sides of the ellipse correspond to zero crossings of the streaking pulse with opposite slopes. Since the shots do not display any irregular structure, they can each be fitted using Gaussian functions, and the width of these functions can be computed. The average breadth of the 300 shots on the left of the ellipse is $\sigma_{\mathrm{L}} = 8.9 \pm 0.2$ eV and that of the 300 shots on the right is $\sigma_{\mathrm{R}} = 9.8 \pm 0.2$ eV. Here and in the following, we have used the standard error on the mean value of N repeated measurements, given by

$$\alpha_{\mathrm{m}} = \frac{\delta}{\sqrt{N}}, \tag{11}$$

where δ is the statistical width of the distribution. We must deconvolve the bandwidth of the field-free photoemission peak σ_{FF} from that of the peak at a zero crossing using the relation

$$\sigma_{\mathrm{DC}} = \sqrt{\sigma_{\mathrm{S}}^2 - \sigma_{\mathrm{FF}}^2} = 7.9 \pm 0.2 \text{ eV.} \tag{12}$$

Here, $\sigma_{\mathrm{s}}^2 = \frac{\sigma_{\mathrm{L}}^2 + \sigma_{\mathrm{R}}^2}{2}$ represents the average of the squares of the mean bandwidth at each zero-crossing. The average field-free photoemission bandwidth is $\sigma_{\mathrm{FF}} = 4.95 \pm 0.01$ eV. The uncertainty on σ_{FF} is much smaller than that on σ_s, because there are many more unstreaked shots available to use in the calculation of the former. The average XFEL pulse duration can be calculated using these quantities, propagating the uncertainties on each one using a standard functional approach. The average full width at half maximum (FWHM) duration of the X-ray pulse is given by

$$\tau_{\mathrm{X}} = 2\sqrt{2\ln(2)} \frac{\sigma_{\mathrm{DC}}}{s} = 7 \pm 1 \text{ fs,} \tag{13}$$

where the factor $2\sqrt{2\ln(2)}$ is used to convert from root-mean-square width to FWHM.

Extraction of the phase shift. As noted in the main text, the two equations

$$x(\theta) = A \sin(\theta + \phi_{\mathrm{A}}), \quad y(\theta) = B \sin(\theta) \tag{14}$$

describe an ellipse and plotting them against each other will allow us to measure ϕ_{A}. A generalized plot of the two equations is shown in Extended Data Fig. 2. In this plot the y intercept, y_1, as well as the maximum value of y, y_2, are highlighted.

From equation (14), it is clear that

$$y_1 = B \sin(-\phi_{\mathrm{A}}), \ y_2 = B. \tag{15}$$

It follows that

$$|\phi_{\mathrm{A}}| = \sin^{-1}\left(\frac{y_1}{y_2}\right). \tag{16}$$

Therefore, we can measure the magnitude of ϕ_{A} simply by measuring the y intercept and maximum value of y in our data. In fact, the same principle can be applied to the negative y intercept and extremum, and both positive and negative pairs on the x axis. All four possible measurements were made and showed little disagreement. For the result shown in the paper, the positive y pair was used. The motivation for choosing y_1 and y_2 as opposed to x_1 and x_2 comes from the fact that our spectral resolution on the photoemission (y) peak is better than that of the Auger peak. Furthermore, x_1 ought to be measured at a zero crossing of the photoemission peak. Under these conditions the peak will be substantially broadened, and its position will be more uncertain. In contrast, the Auger peak—and therefore measurements using points on the y axis, which is at a zero crossing of the Auger peak—is less sensitive to broadening-induced noise.

Error analysis. The method lends itself to straightforward error analysis. If we are able to quantify the uncertainties on y_1 and y_2 as α_1 and α_2 respectively, we could define a parameter $K = \frac{y_1}{y_2}$, whose uncertainty will be given by the following expression:

$$\alpha_K = K \sqrt{\left(\frac{\alpha_{y_1}}{y_1}\right)^2 + \left(\frac{\alpha_{y_2}}{y_2}\right)^2}. \tag{17}$$

From here it is simple to quantify the uncertainty on ϕ_{A} using a functional approach and equation (16), as follows:

$$\alpha_\phi^\pm = \left|\sin^{-1}(K) - \sin^{-1}(K \pm \alpha_K)\right|. \tag{18}$$

Recall that ϕ_{A} corresponds to the streaking phase advance, which occurs between the centres of energy of the photoemission and Auger emission bursts. As described in the main text, the centre-of-mass delay between the two emissions τ_{delay} is a scalar product of ϕ_{A} and the mid-infrared streaking laser wavelength λ_{IR}:

$$\tau_{\mathrm{delay}} = \frac{\phi_{\mathrm{A}} \lambda_{\mathrm{IR}}}{2\pi c}. \tag{19}$$

The constant $2\pi c$ can be assumed to be known to an infinite degree of precision. It is now straightforward to calculate $\alpha_{\mathrm{delay}}^\pm$, the uncertainty on τ_{delay}, which is given by

$$\alpha_{\mathrm{Aug}}^\pm = \tau_{\mathrm{delay}} \sqrt{\left(\frac{\alpha_\phi^\pm}{\phi_{\mathrm{A}}}\right)^2 + \left(\frac{\alpha_\lambda^\pm}{\lambda}\right)^2}. \tag{20}$$

The wavelength λ was measured at Linac Coherent Light Source to be 17^{+1}_{-2} μm. Therefore, we need only identify α_1 and α_2 to determine the precision of our measurement of the centre-of-mass delay. The quantities y_1 and y_2, and their uncertainties, were measured by examining the distribution of data, in particular angular sectors of the ellipse.

Selection of ellipse sectors. It is clear that, when measuring from the origin, the ellipse's y intercept y_1 is contained within a sector aligned with the positive y axis. It is less obvious to determine which sector contains y_2, the maximum value of y.

From the general equation of an ellipse,

$$\begin{pmatrix} x(t) \\ y(t) \end{pmatrix} = \begin{pmatrix} \cos(\alpha) & -\sin(\alpha) \\ \sin(\alpha) & \cos(\alpha) \end{pmatrix} \begin{pmatrix} a\cos(t) \\ b\sin(t) \end{pmatrix} + \begin{pmatrix} x_0 \\ y_0 \end{pmatrix}, \tag{21}$$

one can derive the angle θ_{c} for which y is maximal:

$$\theta_{\mathrm{c}} = \tan^{-1}\left(\frac{b}{a}\cot(\alpha)\right). \tag{22}$$

It follows that $y_2 = y(\theta_c)$. An initial approximation to θ_c was made using a least-squares fit of the elliptical data, which provided the necessary constants α, a and b and resulted in a value of $\theta_{\mathrm{c}}' = 0.6612$ rad. To support this choice of θ_c, y_2 was measured for a range of critical angles θ_c. The results are in Extended Data Fig. 3.

The value of θ_c that maximizes y_2 was found to be very close to that determined from the fit. Furthermore, y_2 shows little variation in the region of θ_c-space close to θ_c'. One can infer that this was a good choice of θ_c, and further that any uncertainty on θ_c' will have a small impact, because it will result in only a small change to y_2.

The next step is to identify y_2 from the distribution of points in the sector at θ_c. The two sectors are highlighted in Extended Data Fig. 4.

Let the sector from which we obtain the value y_i be called Y_i, such that y_i is given by the mean of all the y coordinates of the points in Y_i. The sectors Y_1 and Y_2 are defined in a subtly different way. By definition, y_1 is the y intercept of the ellipse, and as such the sector Y_1 is identified by taking the set of points closest to the y axis, so that

$$Y_1 = \{(x, y) : |x| < \varepsilon_1\}, \ \varepsilon_1 \in \mathbb{R}, \varepsilon_1 > 0. \tag{23}$$

The sector Y_2, conversely, is defined as the points whose angular coordinate is closest to the critical angle θ_c. In terms of polar coordinates, we can define Y_2 as follows:

$$Y_2 = \{(r, \theta) : |\theta - \theta_c| < \varepsilon_2\}, \varepsilon_2 \in \mathbb{R}, \varepsilon_2 > 0. \tag{24}$$

A polar sector is ill-suited for determining y_1, as it incorporates outliers at the edge of the cone, causing the algorithm to overestimate y_1 and therefore ϕ_A when tested with simulated data. However, θ_c is sufficiently large that the boundaries of Y_2 are almost perpendicular to the edge of the distribution, ensuring that few outliers are included. Through repeated tests with simulations, it was verified that a sector of this type results in the most accurate determination of y_2. This sector was also used in the calculation of the pulse duration, as highlighted in Extended Data Fig. 1.

The distributions of y_1 and y_2 obtained from the sectors Y_1 and Y_2 are shown in Extended Data Fig. 5. One can consider the spread of y values inside a sector to be in effect repeated measurements of y_1 and y_2. Therefore, taking the mean of all points in the sector gives a notion of the true values.

The sector Y_1 contains 1,000 points and Y_2 contains 4,000 points. As the number of points increases, the standard error given by equation (11) can be reduced. However, as we make the sectors wider and wider, the width of the distribution δ begins to increase. The sector sizes were chosen to minimize α_M, resulting in uncertainties of around 0.1 eV for y_1 and y_2. The procedure described above can now be used to go from these uncertainties to those of the COE delay τ_{delay}. The dominant source of uncertainty in the experiment is in the measurement of the streaking wavelength, which was only known within a 3 μm range. Accounting for this using equation (20) results in the value of $3.5^{+0.3}_{-0.5}$ fs given in the main text. This value can be interpreted in the context of the quantum theory described in the Supplementary Information; we can simulate the experiment for a range of Auger decay lifetimes and calculate the resulting centre-of-mass delay τ_{delay}. A functional approach allows us to propagate the uncertainties and arrive at our final result of $2.2^{+0.2}_{-0.3}$ fs for the Auger decay lifetime. The uncertainty on this value is that given by the quantum-mechanical model's predictions based on the outer bounds for τ_{delay} and the X-ray pulse duration.

Theory. The theoretical sections of the Supplementary Information present both quantum-mechanical and semiclassical treatments of the experiment. The quantum-mechanical model is used to numerically link the phase shift measured in our experiments with the Auger decay lifetime, whereas the semiclassical model provides a simpler basis for a more intuitive explanation. The former approach is presented in Supplementary Section 1. The foundation of the theory is built upon the time-dependent Schrödinger equation, which describes the photoinduced Auger decay in the dressing field of the optical laser. The propagation of the Auger electron is described within the strong-field approximation. The quantum-mechanical equations allow us to calculate the time-dependent Auger emission profile for a given incident X-ray pulse $\tilde{\varepsilon}_X(t)$ and Auger decay lifetime Γ^{-1}, which is given by the square of the following expression:

$$G_A(t) = \sqrt{\frac{\Gamma}{2\pi}} \exp\left(-\frac{\Gamma}{2}t\right) \int_{t_0}^t dt' \exp\left(\frac{\Gamma}{2}t'\right) \tilde{\varepsilon}_X(t'). \tag{25}$$

Taking into account the interaction of the overlapping optical laser streaking field with the emitted photo- and Auger electrons allows for calculation of the final detected kinetic energies. Altogether, the quantum-mechanical model allows for precise numerical simulation of the entire experiment.

For a more qualitative explanation, a corresponding semiclassical treatment is also presented in Supplementary Section 2. However, it should be emphasized that results presented in the main paper rely only on numerical solutions of the quantum-mechanical model. In this semiclassical approach, making use of the saddle-point approximation, analogous analytical expressions relating the emission times with the final kinetic energies can be derived—the emission time of the Auger electron is a function of the Auger decay lifetime, whereas the photoemission is prompt. The semiclassical approach is built upon further in Supplementary Section 3, in which the relationship between theoretical and experimentally measured quantities is discussed. With the aid of appropriate assumptions, the emission time–kinetic energy relations from Supplementary Section 2 are used to arrive at the following expressions for the streaking laser-induced kinetic energy shift of photoelectrons and Auger electrons, respectively:

$$\Delta E_{ph} \approx k_0 A_{IR}(t_0) = A_0 \sqrt{2E_{ph}} \sin(\omega_{IR} t_0). \tag{26}$$

$$\Delta E_{Auger} \approx k_0 A_{IR}(t_0 + C_{TA}) = A_0 \sqrt{2E_A} \sin(\omega_{IR} t_0 + \phi), \tag{27}$$

where C_{TA} is the centre of time of the Auger emission profile and $A_{IR}(t)$ is the vector potential of the streaking laser field that induces the change in kinetic energy. Equation (26) is in fact equivalent to equation (3) from the main text. Supplementary Section 3 also uses the difference in emission times for the photoelectrons and Auger electrons to calculate a time delay, which itself results in a phase shift in the streaking measurements. This phase shift is directly measured in the experiment, and it is also the key output parameter of the original full quantum-mechanical numerical simulation: for a given set of experimental parameters, each Auger decay lifetime results in a unique value of the phase shift. To determine the Auger decay lifetime, it is iterated over until the simulated phase shift matches the observed phase shift, as described in the main text.

Data availability
The data that support the plots within this paper and other findings of this study are available from the corresponding authors on request.

Code availability
Interested parties may contact A.K.K. (kazan356@rambler.ru) to obtain a copy of the simulation code used to verify the quantum treatment of Auger decay for our experiment.

References
53. Helml, W. et al. Measuring the temporal structure of few-femtosecond free-electron laser X-ray pulses directly in the time domain. *Nat. Photon.* **8**, 950–957 (2014).
54. Behrens, C. et al. Few-femtosecond time-resolved measurements of X-ray free-electron lasers. *Nat. Commun.* **5**, 3762 (2014).

Author contributions
L.F.D. and G.D. proposed the measurement of Auger lifetimes at the Linac Coherent Light Source and A.L.C. conceived the self-referenced streaking approach that enabled these measurements. The experiment and supporting experiments were performed by A.A.-H., C. Bostedt, J.B., H.B., M.B., A.C., S.C., A.L.C., R.C., J.T.C., L.F.D., G.D., K.F., I.G., D.C.H., M.C.H., M.I., R.K., A.R.M., F.T., W.H., T. Mazza, M.M., H.P., C.R., A.S., P.A.W., M.W. and K.Z. The mid-infrared laser for streaking was provided by M.C.H. and J.R. Electron beam tuning and diagnostics were provided by Y.D., T. Maxwell and C. Behrens D.C.H., C. Bostedt, W.H., N.M.K., A.K.K., M.M., H.S., G.D., C. Behrens and A.L.C. were primarily responsible for interpreting the experimental results. D.C.H., M.W., A.S., A.C., R.S., C.Behrens and A.L.C. analysed the data. N.M.K. and A.K.K. performed theoretical calculations. D.C.H., C. Bostedt, C. Behrens and A.L.C. were primarily responsible for writing the paper. All authors contributed to the final version of the manuscript.

Competing interests
The authors declare no competing interests.

Additional information
Extended data is available for this paper at https://doi.org/10.1038/s41567-020-01111-0.

Supplementary information is available for this paper at https://doi.org/10.1038/s41567-020-01111-0.

Correspondence and requests for materials should be addressed to D.C.H. or A.L.C.

Peer review information *Nature Physics* thanks Lorenz Cederbaum, Markus Guehr and the other, anonymous, reviewer(s) for their contribution to the peer review of this work.

Reprints and permissions information is available at www.nature.com/reprints.
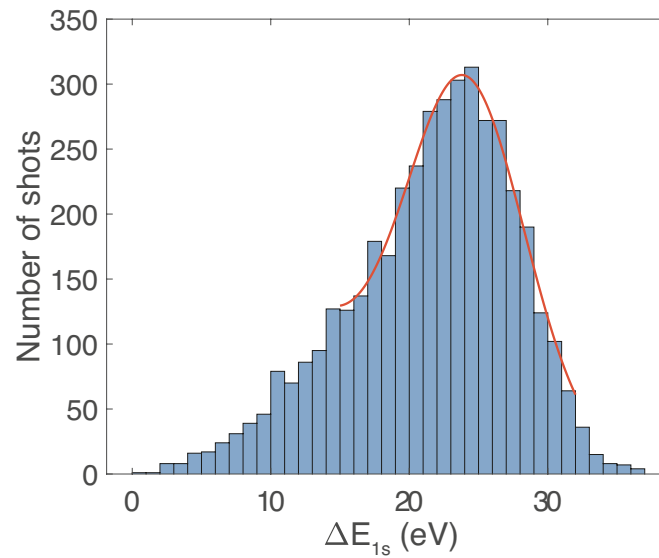
Extended Data Fig. 1 | Distribution of maximally streaked kinetic energies. The changes in photoelectron kinetic energy in the sector corresponding to maximal streaking phase are plotted in the histogram. The red line shows the numerically determined least-square fit, from which we extract the peak of the distribution. By the normally distributed nature of timing jitter, highest number of shots will overlap at or near the peak of the pulse envelope, so that the peak of the histogram ought to correspond to those conditions.
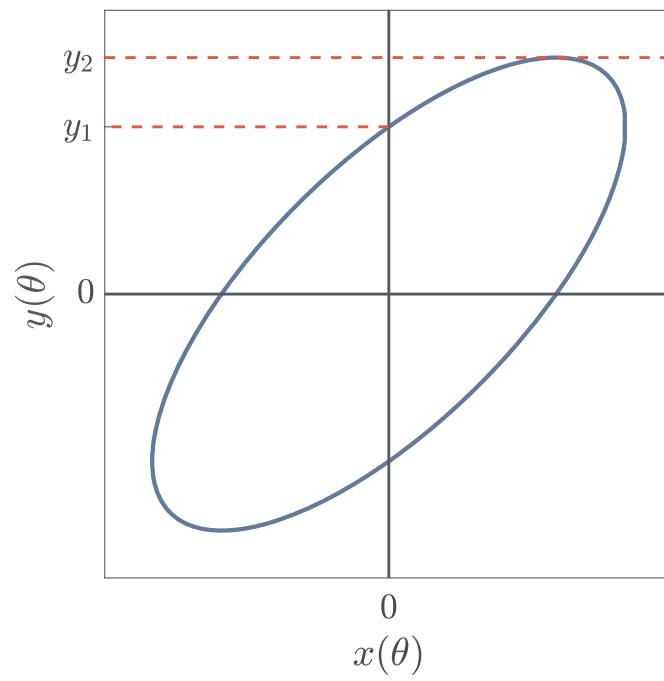
Extended Data Fig. 2 | Generalized ellipse. An arbitrary ellipse is shown (blue line) with the *x*- and *y*-axes highlighted (black lines), in addition to the parameters y_1 and y_2 (red dotted lines).
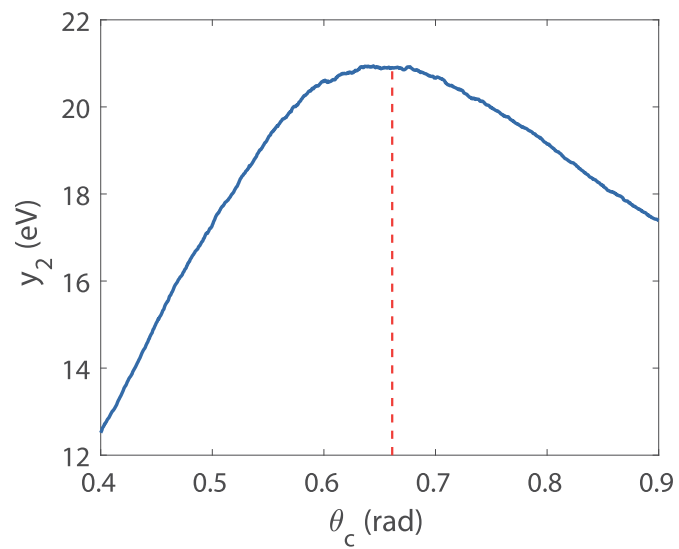
Extended Data Fig. 3 | Critical angle θ_c. The measured value of y_2 is shown (blue line) for a range of critical angles θ_c. The red dotted line represents the value of θ_c that was used in the final analysis.
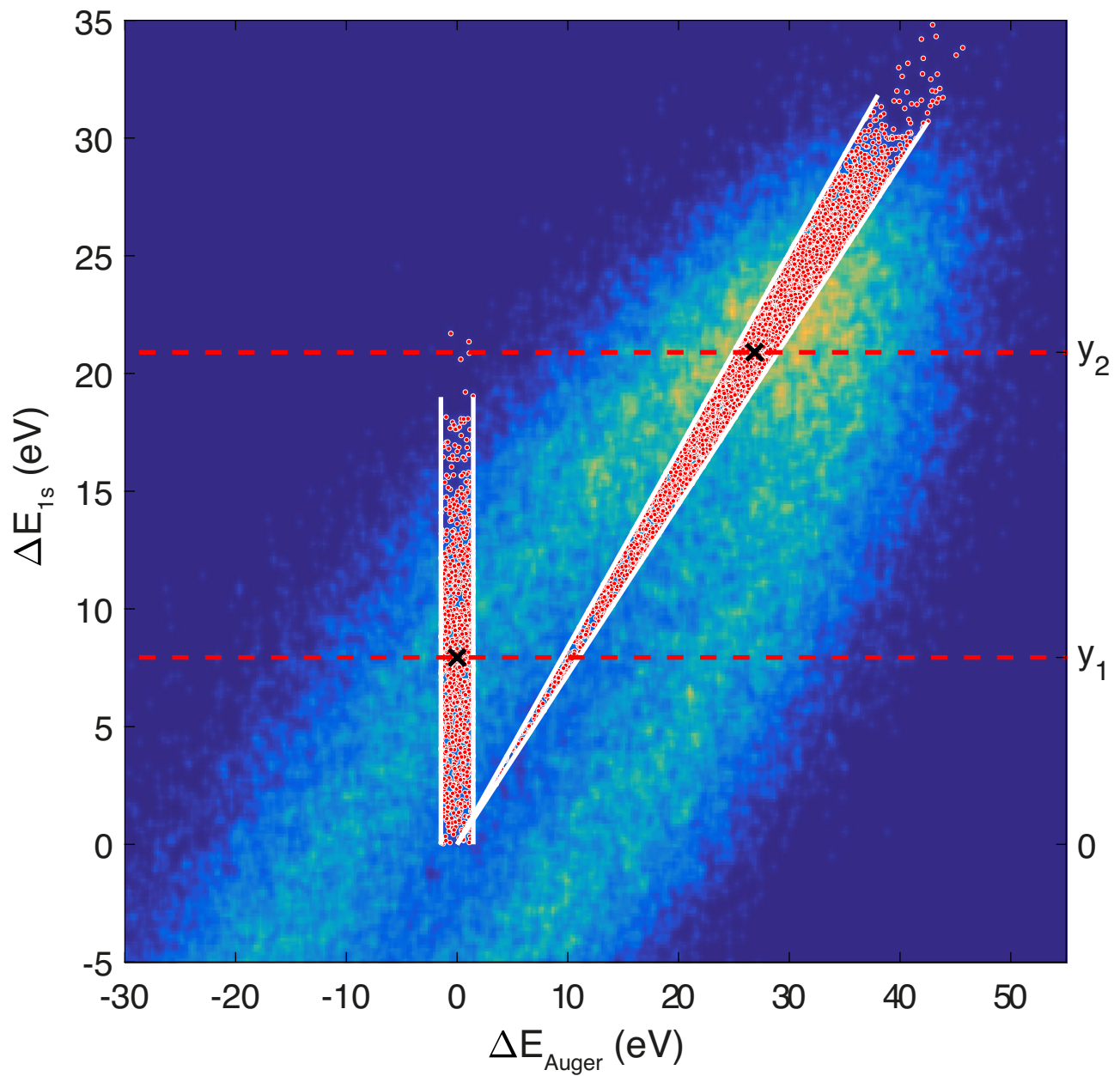
Extended Data Fig. 4 | Sectors for calculation of the parameters y_1 and y_2. A zoomed-in section of the data is shown. Overlaid on the density map, the red points are those contained in each of the sectors used to find the parameters. The black crosses represent the measured values y_1 and y_2, which are highlighted by the red dotted lines. From these data, y_1 and y_2 were measured at 7.9 eV and 20.9 eV respectively.
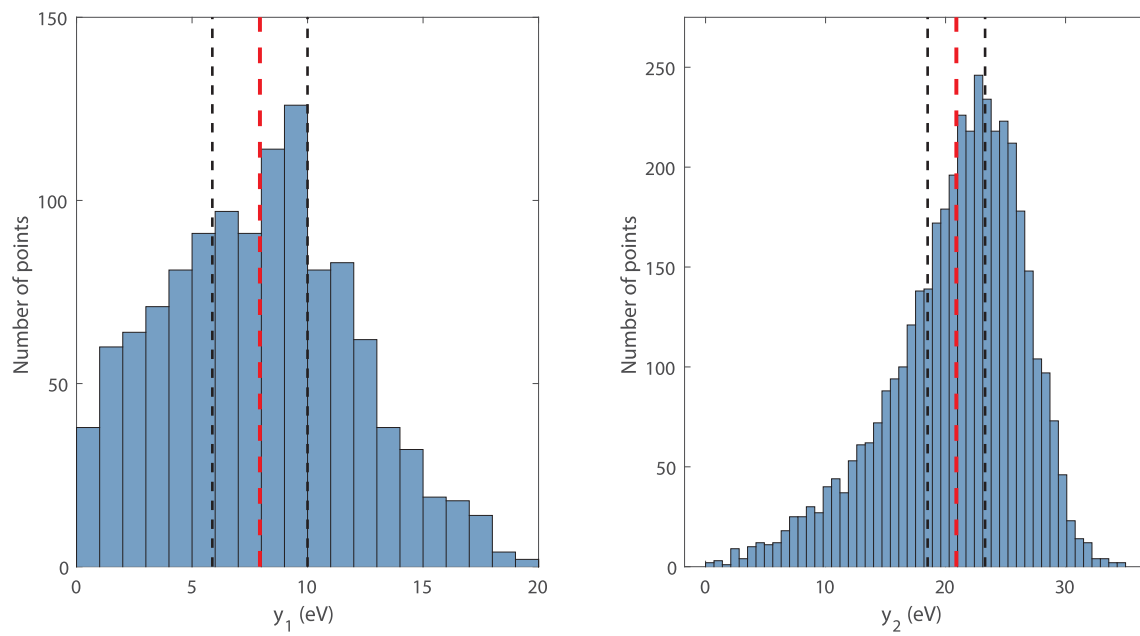
Extended Data Fig. 5 | The distribution of parameters y_1 and y_2. The red dashed lines highlight the mean value and the black dashed lines display the statistical width of each distribution.